Acta Materialia 218 (2021) 117095

Contents lists available at ScienceDirect

Acta Materialia

journal homepage: www.elsevier.com/locate/actamat

Full length article

Mechanical properties of CrN-based superlattices: Impact of magnetism

L. Löfler[a,b,*], R. Hahn[b], P.H. Mayrhofer[b], M. Bartosik[b], D. Holec[a]

[a] Department of Materials Science, Montanuniversität Leoben, Leoben, Austria
[b] Institute of Materials Science and Technology, TU Wien, Vienna, Austria

ARTICLE INFO

Article history:
Received 20 March 2021
Revised 9 June 2021
Accepted 12 June 2021
Available online 1 July 2021

Keywords:
Multilayer
DFT
Fracture toughness

ABSTRACT

Superlattices represent an important design concept for materials with exceptional properties. In this work, we report on the influence of different interface orientations and magnetic configurations of CrN in B1 CrN/(TiN,AlN) superlattices on their mechanical and the structural properties studied with the help of density functional theory. The oscillations of interplanar spacings, formerly linked to the cleavage strength in similar material systems, were found to be in no correlation with the magnetic moments of individual CrN planes. An explicit consideration of the interfaces is important for an accurate estimation of elastic constants. In this context, the continuum mechanics-based Grimsditsch and Nizzoli method ignoring interface properties yields even qualitatively wrong results. Similarly, our calculations show that the ferromagnetic state of CrN as an approximation of (computationally much more demanding) paramagnetic magnetic state does not provide correct predictions of the material behaviour. In other words, explicit treatment of the magnetic moments as well as the interfaces is necessary for qualitatively correct modelling of CrN-based superlattices. Finally, the theoretically predicted elastic constants and fracture toughness values were corroborated by CrN/TiN micro-cantilever experiments.

1. Introduction

Ceramic thin film coatings are commonly used to enhance properties of components to withstand the ever-increasing requirements of modern applications [1]. In many cases both high hardness and fracture toughness are sought after, which are, however, often mutually exclusive [2].

The protective hard coatings are typically synthesized by either physical vapor deposition (PVD) or chemical vapor deposition (CVD) [3]. Several approaches can be used to tune the coating's properties during the coating process. Considering monolithic films, the material composition can be fine-tuned by additional alloying element(s) or controlled defect concentration to enhance various functional properties such as oxidation resistance [4–7] or thermal stability [8–11]. Microstructural design concepts include nanocomposite coatings [12–15], superlattice/multilayer coatings [16–19] or advanced (hierarchical) architectures [20–22]. We note that the references given above are by far not exhaustive, and should serve the reader as a starting point for further exploring the rich existing literature. Importantly, each of the above mentioned categories contains simulation/modelling contributions, demonstrating their role in modern materials science.

The superlattice/multilayer configurations consist of layers of alternating materials and often show improved properties. These layers share a common lattice and contain (semi-)coherent interfaces in the former case of superlattices. Already in 1987, Helmersson et al. [16] showed that TiN/VN multilayers exhibit an increased hardness compared to bulk TiN. Similar trends were reported also for CrN/AlN [23], TiN/CrN [17], TiN/WN [18] and MoN/TaN [19]. Later studies on superlattices showed an additional increase of the coating's fracture toughness peaking at certain bi-layer periods depending on the combined materials, TiN/CrN [17], TiN/WN [18] or MoN/TaN [19]. The nature of these coatings, namely a small bi-layer period for which the enhancement of the mechanical properties is observed, introduces a significant amount of "interface material". This is the interface between the individual layers and its nearest neighbourhood, which significantly differs from the bulk by the broken (chemical) symmetry on both sides of the interface. Therefore, it is expected to play a key role for determining both the hardness and the fracture toughness of superlattices and small bi-layer period multilayers. The exact mechanisms behind the outstanding mechanical properties is however not yet fully understood.

* Corresponding author.
E-mail address: lukas.loefler@tuwien.ac.at (L. Löfler).

https://doi.org/10.1016/j.actamat.2021.117095

In the present paper we aim on exploring in detail the superlattice coatings, for which quantum mechanical calculations are well suited, as well as are relatively easy realizable experimentally. Tensile strength of nitride superlattices has been theoretically studied previously for TiN/VN [24,25], AlN/VN [25], TiN/AlN [25,26] (including wurtzite phase of AlN), and MoN/TaN [19,27] (including the impact of point defects). These studies included also discussion on structural and mechanical properties of superlattices. Systematic exploration of nitride-based superlattices was presented by Wang et al. [28].

None of the above mentioned theoretical papers, however, dealt with CrN, which is another commonly used system for hard coatings exhibiting structural compatibility with TiN (and B1 cubic AlN), good hardness and oxidation resistance. CrN exhibits different magnetic configurations depending on temperature: it has an anti-ferromagnetic (afm) order with (110) double-planes of alternating spins in its ground state CrN [29], enforcing the structure to be orthorombic with lattice constants of 5.71, 2.99 and 4.07 Å. Above the Neél temperature of ≈280 K, CrN undergoes a phase transformation to paramagnetic (pm) state with rock-salt B1 structure [30]. Zhou et al. [30] also showed that an artificial ferromagnetic (fm) state of CrN is a reasonable approximation to computationally very expensive pm-CrN regarding its mechanical properties. Structural properties of CrN/AlN superlattices were reported by Zhang et al. [31], whereas Friák et al. [32] focused on elastic properties; both works include synergy of theory with experiment.

However, a systematic study on the interface-related properties in CrN-based superlattices is missing. In this work we investigate the influence of different interface orientations and magnetic states on the mechanical properties including the tensile strength and fracture toughness of CrN/AlN and CrN/TiN superlattices. All three nitrides (CrN, AlN, TiN) are already commonly used in coatings, making them prime candidates for pairing them together. Their nitrides were considered to be cubic. TiN and pm-CrN are naturally crystallizing in the cubic B1 rocksalt structure, AlN has a B4 hexagonal wurzite structure in its ground state. In combination with other nitrides, AlN can be stabilized in the B1 structure in multilayers for thin layer thicknesses [23,33,34]. The cubic lattice parameters are a_{AlN}=4.07 Å [35], a_{CrN}=4.14 Å [36] and a_{TiN}=4.24 Å [37], hence probing also different in-plane stress states in CrN in the superlattices: tensile in CrN/TiN and compresive in CrN/AlN. Our primary tool is Density Functional Theory (DFT) and the theoretical results are corroborated by experimental results and are discussed in the light of existing literature data.

2. Methods

The calculations were performed in the framework of Density Functional Theory (DFT) as implemented in the Vienna Ab initio Simulation Package (VASP) applying a plane wave basis set [39,40] using the generalized gradient approximation (GGA) for the exchange-correction effects. The cutoff energy was set to 600 eV and an automatic k-point mesh with 60 points was used. As convergence criteria an energy difference of 10^{-5} eV (per simulation box) and atomic forces less then 10^{-4} eV/Å were chosen. The starting moment of the Cr atoms was set to 2.3 μ_{b}. The paramagnetic (pm) state of CrN was modeled with a Special Quasi-random Structure (SQS) [41], distributing the positive and negative spins in a $2\times2\times2$ supercell. The antiferromagnetic (afm) nature of CrN changes the unit cell from cubic to orthorombic as described in [29]. Consequently the sides of the cell differ not only structurally but also magnetically. The used unit cell can be seen in Fig. 1. For the paramagnetic superlattice, $2\times2\times4$ supercells containing 160 atoms were used, where as $1\times1\times4$ supercells were used for the afm and ferromagnetic (fm) configurations. The fm state of CrN was considered as a computationally cheaper alternative for representing the pm cells [30], which is to be tested for its applicability.

To calculate the elastic response of the different structures, the strain-stress method was used [42]. The resulting general stiffness tensor was then projected onto the crystal symmetry of the structure following the formalism described by Moakher and Norris [43]. The Voigt-Reuss scheme as implemented in SC-EMA [44,45] was used for homogenization to get values comparable with experiments. In addition, the binary stiffness constants were used to approximate those of the superlattices with the approach of Grimsditsch and Nizzoli (G&N)[46].

The tensile strength was determined by cleaving the supercells at different planes. This was done by introducing vacuum with a gradually increasing thickness between two planes until the atoms in the so-created (rigid) blocks had no interaction, i.e. the total energy of the system was constant. The resulting energy curve was fitted with Rose's universal binding relation [24,47]:

$$\Delta E(x) = \frac{E(x)-E_0}{A} = E_c A\left[1-\left(1+\frac{x}{l_{\mathrm{crit}}}\right)\exp\left(-\frac{x}{l_{\mathrm{crit}}}\right)\right] \tag{1}$$

where x is the induced separation (vacuum) between the cleaved planes and E_0 is the ground state total energy. Cleavage energy, E_c, and critical length, l_{crit}, are two fitting parameters describing the cleavage to be determined. Deriving Eq. (1) yields the critical stress, σ_{crit}:

$$\sigma_{\mathrm{crit}} = \left.\frac{dE(x)}{dx}\right|_{x=l_{\mathrm{crit}}} = \frac{E_c}{l_{\mathrm{crit}}e} \tag{2}$$

The cleavage energy is the energy required to separate the cell into two rigid blocks along the given plane. The critical length and stress are two values to determine the actual strength of the plane: the maximum stress the system can withstand in tension is σ_{crit}, and it corresponds to the separation l_c. To ensure no interaction of the interface with itself, a certain cell size is needed. Tests have shown that a supercell composed of 12 planes parallel to the cleavage plane is sufficient for the two surfaces to not interact with each other over the periodic boundary conditions. In such case, each material is represented by six planes. The maximum separation of 10 Å was considered; the total energy changes for larger separations were negligible.

The fracture toughness (K_{IC}) was determined from the calculated cleavage energy (E_c), supercell cross-section area along the cleavage plane, A, and the directional Young's modulus, E_{hkl}, in a direction perpendicular to the cleavage plane, following the formula from [48]:

$$K_{\mathrm{IC}} = \sqrt{4E_cE_{hkl}} \tag{3}$$

In the original formula, the term E_c was represented by surface energy, γ. Tests on the present systems showed that γ can be well approximated by the cleavage energy, which is, in fact, unrelaxed surface energy.

Using the Voigt's notation for C_{ij} being the matrix representation of the elastic constants tensor c_{ijkl}, the compliance matrix, S_{ij} is calculated as inverse of the C_{ij} matrix. The directional Youngs's moduli were calculated using the equations derived in Ref. [49] for cubic and orthorhombic systems:

$$\frac{1}{E^{\mathrm{cub}}_{hkl}} = S_{11} - 2\left(S_{11}-S_{12}-\frac{1}{2}S_{44}\right)(\bar{h}^2\bar{k}^2+\bar{k}^2\bar{l}^2+\bar{h}^2\bar{l}^2) \tag{4}$$

$$\begin{aligned}\frac{1}{E^{\mathrm{ortho}}_{hkl}} = {} & \bar{h}^4S_{11}+2\bar{h}^2\bar{k}^2S_{12}+2\bar{h}^2\bar{l}^2S_{13}+\bar{k}^4S_{22}+2\bar{k}^2\bar{l}^2S_{23}+\bar{l}^4S_{33}\\ & +\bar{k}^2\bar{l}^2S_{44}+\bar{h}^2\bar{l}^2S_{55}+\bar{h}^2\bar{k}^2S_{66},\end{aligned} \tag{5}$$

where $[\bar{h}\,\bar{k}\,\bar{l}]$ is a normalized vector in the crystallographic direction $[hkl]$.

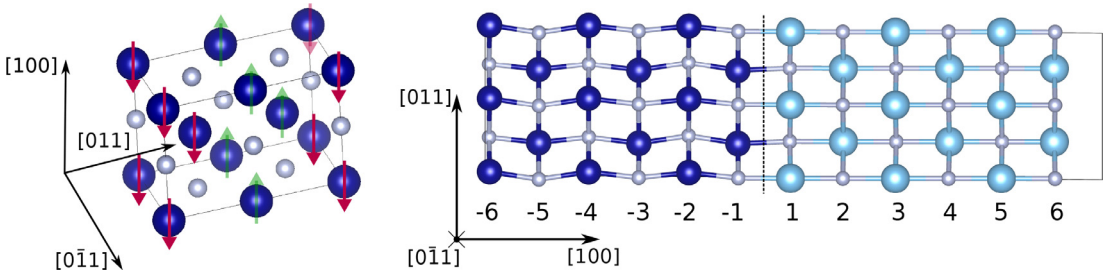

Fig. 1. The left-hand panel shows antiferromagnetic CrN in its orthorhombic cell, the spin distribution in the Cr atoms is indicated by the coloured arrows. The right-hand panel shows one of the used supercells, in this case CrN/TiN with a (100) interface. The numbers below indicate the plane-indexing used throughout this manuscript. The structures were visualized using the VESTA3 software [38].

Table 1
Overview of the different systems investigated in this study. CrN was paired either with TiN or AlN and investigated for different interface orientations as well as magnetic configurations. ⊥ indicates that only the direction perpendicular to the interface was investigated.

material	interface	magnetic conf. (CrN)
CrN/TiN	(100)	pm (⊥), fm, afm
CrN/TiN	(011)	fm, afm
CrN/AlN	(100)	fm, afm
CrN/AlN	(011)	fm, afm

Finally, Table 1 gives an overview of the different superlattice configurations considered in the present work, namely, superlattice with interfaces parallel to crystallographic (100) and (011) planes. The former yields afm planes (in CrN) with a total spin 0 μ_B parallel to the interface, whereas the latter case leads to magnetically polarized planes.

3. Results

3.1. Structural characterization and magnetic behavior

The superlattice configurations result in the atoms to slightly change their positions, and consequently also other properties change compared with the parent binary bulk phases. Figs. 2 and 3 show the mean of the absolute values of magnetic moments (per metal atom, blue solid lines), the mean magnetic moments (per metal atom, blue dash-dotted lines) for each individual plane as well as the interplanar spacing between the planes (green lines). Clearly, AlN and TiN exhibit no magnetism (only negligibly small magnetic moments near the interfaces with adjacent CrN). The mean absolute magnetic moments per Cr atom in the CrN planes are $\approx 2.30\mu_B$ and $\approx 2.35\,\mu_B$ for (100) and (110) interfaces, respectively, which is somewhat lower than reported for bulk pm-CrN ($2.48\,\mu_B$ in Ref. [30]) and a little higher than the values calculated here for the bulk afm-CrN $2.27\mu_B$. Moreover, the magnitude of the magnetic moment seems to be independent of the chosen magnetic ordering, either fm or afm. N atoms in CrN layers do show negligibly small magnetic moments of $\approx 0.05\,\mu_B$, and are hence considered also non-magnetic. It is worth noting that while the magnitude of the magnetic moment is almost constant in the case of the afm configuration, it shows a depth profile for the fm ordering. This behaviour is the same for TiN/CrN as well as for AlN/CrN, and also for different interface orientations (100) in Fig. 2 and (011) in Fig. 3. However, while the magnetic moment is higher at the (100) interface than in the middle of the fm-CrN layer, the (110) interface has a slightly lower magnetic moment than the bulk of the fm-CrN layer. The profile of the magnitude of magnetic moments is symmetrical with respect to the center of the CrN layers. The mean absolute value of magnetic moment of Cr atoms is slightly higher in the fm state than in the afm state in the case of (100) interfaces, while the opposite holds for the (011) orientation. Nevertheless, the differences are below $0.04\,\mu_B$/at., a value which is negligibly small. Therefore we can conclude that the magnitude of the magnetic moment is independent of the actual magnetic ordering (fm or afm).

An interesting behaviour is nonetheless revealed when inspecting the mean value of the magnetic moment (dash-dotted lines in Figs. 2 and 3). Considering the spin arrangement in (100) planes (right-hand panel of Fig. 1), the mean value of the spin in the (100) plane is 0 in the case of the afm state, and non-zero in the case of the fm state where both Cr atoms are symmetry-equivalent and thus yield the same spin. While the fm-(100)CrN/TiN shows the expected behaviour, in which all spins have the same orientation, the mean value of the (100) planes in fm-(100)CrN/AlN alternates between positive and negative values. This result implies that the final magnetic state consists of (100) planes with alternating spins, i.e. some kind of an antiferromagnetic order. We note that this afm-(100) state is different from the CrN afm ground state with double-(011) planes. The meta-stability of the false afm state (denoted as fm in the present manuscript) is further underlined by the formation energy being 24 meV/at. higher than the (100)CrN/AlN superlattice with the true afm state (Fig. 2d).

In conclusion, the presence of the (100) interface between CrN and AlN induces a perturbation to the system strong enough to lead to a spontaneous flipping of magnetic moment on some Cr atoms and hence inducing a false afm configuration. We speculate that this is driven by CrN trying to rearranging its magnetic order to be “closer” to its true afm ground state [29].

The interplanar spacings follow a similar picture as the magnetic moments in the sense that they exhibit symmetrical behaviour in most of the cases. The small asymmetry of afm-(100)CrN/TiN can be attributed to numerical errors, the values of interplanar distances between CrN (100) planes number 2 and 3, and 4 and 5 are identical within the accuracy of our calculations (Fig. 2a). In general, the oscillations of interplanar spacings are smaller in AlN than in CrN, in agreement with experimental observations and explicit calculations on pm-CrN/AlN [31]. Such behaviour was explained by different extend of Friedel oscillations in metallic and semiconducting systems [25,26,31]. Regarding the CrN/TiN superlattices, the variations of the interplanar spacings are more pronounced in the case of CrN than TiN, and in the case of (011) than (100) interfaces. Importantly, the minima of the interplanar distances often correlate with the adjacent planes being spin-polarized and having opposite mean spins (e.g., fm-(100)CrN/AlN or afm-(001) CrN/TiN or afm-(001)CrN/AlN). This points towards a strong magnetic interaction and an interplay between the magnetic and structural properties of CrN.

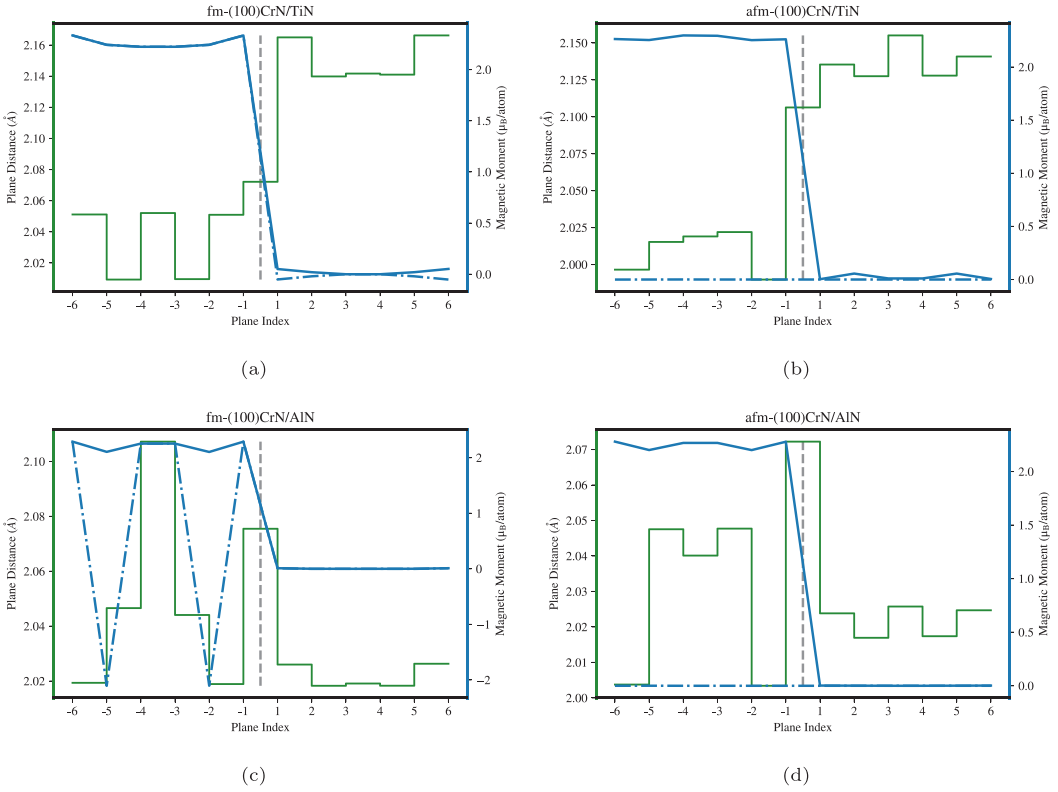

Fig. 2. Mean values of the absolute values of the magnetic moments in each plane (per metal atom, blue solid lines), mean magnetic moment in plane (per atom, dash-dotted blue line) and interplanar spacing (green lines) for superlattices with (100) interfaces: a) fm-CrN/TiN, b) afm-CrN/TiN, c) fm-CrN/AlN, d) afm-CrN/AlN. (For interpretation of the references to colour in this figure legend, the reader is referred to the web version of this article.)

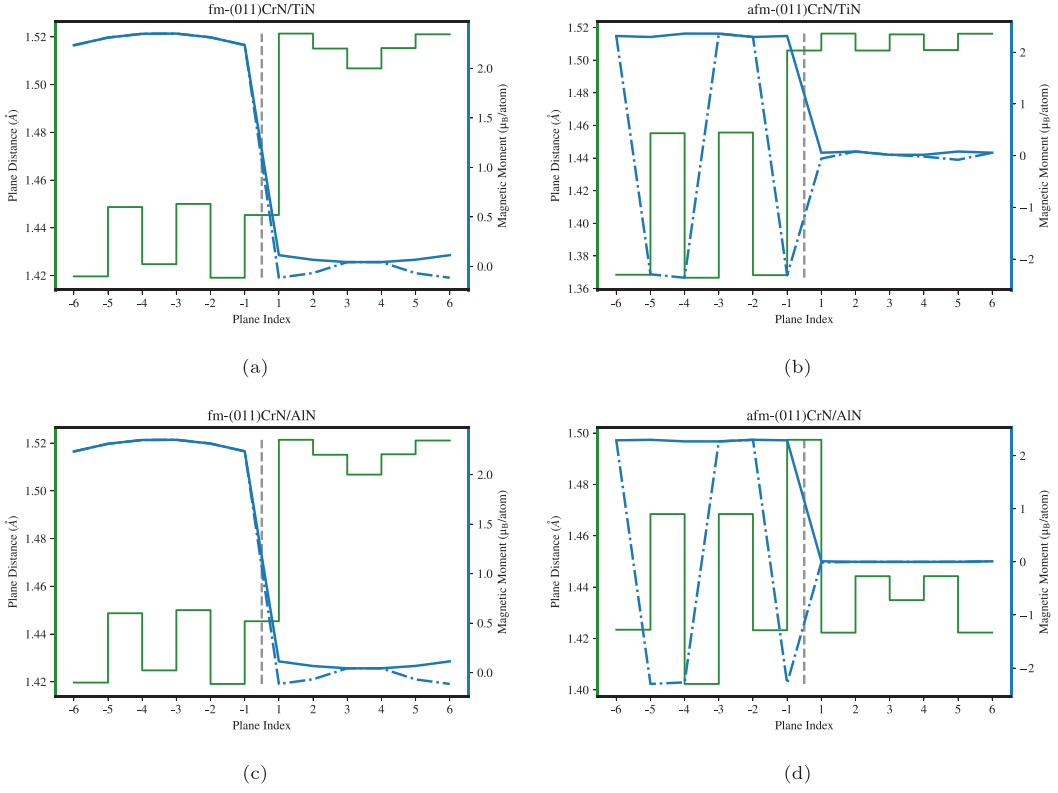

Fig. 3. Mean values of the absolute values of magnetic moments in each plane (per metal atom, blue solid lines), mean magnetic moment in plane (per atom, dash-dotted blue line) and interplanar spacing (green lines) for superlattices with (011) interfaces: a) fm-CrN/TiN, b) afm-CrN/TiN, c) fm-CrN/AlN, d) afm-CrN/AlN. (For interpretation of the references to colour in this figure legend, the reader is referred to the web version of this article.)

Table 2
Stiffness constants of the supercells for (100) and (110) interface as well as those of binaries. They were calculated using the strain/stress method. In addition the binaries were used to calculate the elastic constants of the supercells using the Grimsditsch and Nizzoli approach, they are marked with G&N in the table.

System	C_{11} (GPa)	C_{22}	C_{33}	C_{44}	C_{55}	C_{66}	C_{12}	C_{13}	C_{23}
conventional coordinate system									
	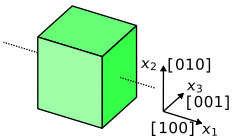								
TiN	608	-	-	159	-	-	143	-	-
afm-CrN	481	560	560	137	99	99	118	118	145
AlN	416	-	-	308	-	-	158	-	-
(100) interface									
	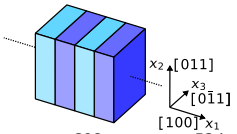								
TiN	608	534	534	232	159	159	143	143	215
afm-CrN/TiN	564	483	428	188	114	138	131	144	171
afm-CrN/TiN G&N	537	540	484	220	112	132	129	129	215
fm-CrN/TiN	450	430	430	177	111	111	256	256	191
pm-CrN/TiN	540	478	478	191	121	121	266	266	209
afm-CrN	481	546	434	207	86	113	118	118	215
afm-CrN/AlN	474	549	486	162	151	175	141	149	98
afm-CrN/AlN G&N	447	570	514	168	134	165	140	140	97
fm-CrN/AlN	440	480	480	133	112	112	307	307	106
AlN	416	596	596	129	308	308	158	158	-21
(011) interface									
	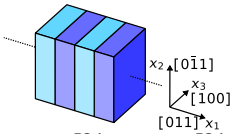								
TiN	534	534	608	159	159	232	215	143	143
afm-CrN/TiN	467	518	535	136	104	205	190	144	153
afm-CrN/TiN G&N	540	484	544	123	132	219	215	131	131
fm-CrN/TiN	426	476	490	125	111	166	175	126	135
afm-CrN	546	434	481	86	113	207	215	118	118
afm-CrN/AlN	505	511	477	202	96	148	118	146	146
afm-CrN/AlN G&N	502	544	448	210	134	159	116	135	143
fm-CrN/AlN	427	412	334	181	134	127	113	326	139
AlN	596	596	416	308	308	129	-21	158	158

Overall we can conclude that, despite some differences depending on the actual magnetic order, the *structural properties* of both magnetic configurations (nominally fm and afm) for both systems and each of the both interface orientations are rather similar.

3.2. Elastic constants

The stiffness constants calculated using the strain-stress method are listed in Tab. 2 for the different configurations. For the superlattices, the axis '1' is perpendicular to the interface, i.e., C_{11} relates $\sigma_{\perp\perp}$ and $\epsilon_{\perp\perp}$, and $\perp=$ [100] and $\perp=$ [011] directions in the conventional cubic reference frame in the case of (100) and (011) interfaces, respectively. The other two axes '2' and '3' coincide with the (orthogonal) sides of the simulation box. The orthorhombic nature of the afm-CrN is reflected in the orthorhombic symmetry[1] of the stiffness tensor, while those of AlN and TiN keep the cubic symmetry. The results for TiN and AlN are in agreement with other studies [50,51]; also C_{ij} of afm-CrN are similar to the ones calculated by [30,52]. We note that C_{ij} of afm-CrN is also expressed in the coordination frame connected with the underlying conventional cubic system of the rock-salt structure; elastic constants in the orthothombic system (as used e.g. by [30], see Fig. 1a) correspond to those listed for the (100) and (0$\bar{1}$1) interfaces.

[1] The apparent tetragonal symmetry of the stiffness tensor matrix is due to rounding the values to GPa.

There is a principal difference between the CrN/TiN and CrN/AlN superlattices, stemming from the elastic symmetry of its binary compounds, as visualized using directional Young's modulus E_{hkl}. While TiN exhibit maximum of E_{hkl} for the [100] direction (and minimum for the [111] direction), AlN shows exactly the opposite trend. The three ⟨100⟩ directions are not all equivalent in the case of CrN due to the antiferromagnetic order, however, also in this case the $E_{[100]}$ is larger than $E_{[0\bar{1}1]}$ and $E_{[011]}$, i.e. shows similar behaviour as TiN. These trends are visualized by the dashed lines in Fig. 4 for all three binaries and different projections.

The directional dependence of an superlattice-effective Young's modulus is shown with the thick solid lines. It turns out, that afm-CrN/TiN elastic response is mostly "in-between" of afm-CrN and TiN (the solid blue line is between the blue and green dashed lines in Fig. 4). This holds true for both interface orientations. However, it is worthwhile noting some exceptions to the above described behaviour. Notably, the [011] direction (i.e. the direction along which Cr planes with constant spin are alternating, see Fig. 1) in the SL is softer than any of the binary TiN (435 GPa) and afm-CrN (432 GPa). Moreover, in the case of (100) interface, the SL [010] and [001] directions (diagonal directions in the panel labelled "interface plane") are also clearly softer than both binary constituents. Nevertheless, there are no directions in which the SL Young's modulus outperforms both TiN and afm-CrN at the same time.

The situation is slightly more complicated for the case of afm-CrN/AlN SL due to different elastic response. Consequently, the SL

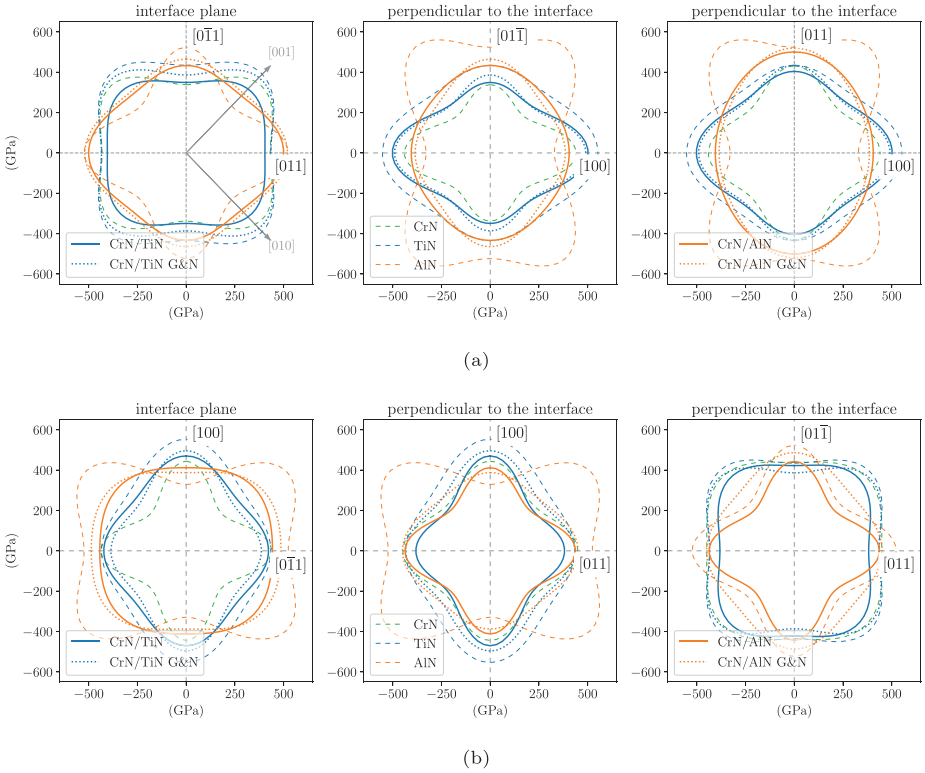

Fig. 4. Directional Young's modulus for the three main projection planes of afm-CrN/TiN and afm-CrN/AlN with a) (100) and b) (011) interfaces.

Young's modulus is much more isotropic (less directional) than each of the constituents, as well as in comparison to the afm-CrN/TiN SL (compare the solid orange and blue lines for the (100) interface).

Lastly, the Grimsditsch&Nizzoli approach [[46]] was applied to estimate the elastic constants of the superlattices, in addition to the explicit strain-stress method. The G&N method is very fast since it works only with the elastic constants of the constituents as inputs. The resulting values are provided in Tab. 2 along with the properly rotated C_{ij} of binaries and respective SLs. Despite the fact that the individual C_{ij} from the G&N and the stress-strain method differ by up to $\approx 20\%$ in extreme cases (see, e.g., C_{23} for afm-CrN/TiN), the resulting directional dependence of the Young's modulus seems to satisfactorily agree (compare dotted and solid lines in Fig. 4). The agreement is particularly good for the afm-(100)CrN/AlN system, which has been already reported before: Friák et al. [32] showed not only excellent agreement between the two theoretical approaches, but also a quantitative agreement with indentation modulus of highly orientated coherent CrN/AlN superlattices. Nevertheless, the present comparison also points out deficiencies of the G&N method. Firstly, the resulting $E_{hkl}^{\mathrm{G\&N}}$ is always "in-between" the values of the constituting binaries. Therefore, it fails to reproduce the SL softening in some directions (e.g., [010] or [001] of afm-CrN/TiN), or slightly superior stiffness of the SL compared with the constituents (e.g., direction tilted by $\approx 20^{\circ}$ away from the [100] direction towards the [0$\bar{1}$1] direction in the afm-(100)CrN/AlN SL, see Fig. 4a, middle panel). We conclude that such effects stem from the interfaces, which are explicitly included in the stress-strain method but ignored by the G&N method. Consequently, the G&N method should be applied with a great care in the case of small bi-layer periods (high density of interfaces).

Young's modulus of different magnetic orderings in CrN/TiN and CrN/AlN SLs are plotted in Fig. 5 for both considered configurations. The motivation for this investigation was a suggestive conclusion of Ref. [30], which showed that fm-CrN is dynamically stable, and hence may serve as an approximation of cubic pm-CrN. Comparing the elastic properties visualized using the Young's modulus, several conclusions can be drawn. Firstly, the pm-CrN/TiN is elastically "between" afm-CrN/TiN and fm-CrN/TiN (100)-orientated SL, with the afm (fm) configuration being systematically stiffer (softer) than the pm state. Secondly, the fm-CrN/AlN configuration shows significant anisotropy, which could point towards reduced mechanical stability (very small values of Young's modulus in some directions). This is the case particularly for the (011) interface in which the fm state was stabilized (see Fig. 3c). Nevertheless, since fm-CrN/TiN does not exhibit any significant elastic instability, it is not purely the magnetic state, but rather the magnetic state together with the interface, which results into high elastic anisotropy. Finally we note, that a decent agreement between C_{ij} of pm-CrN and fm-CrN was obtained only in the case of GGA+U approach; pure GGA exchange-correlation potential yielded largely different tensor of elastic stiffnesses [30].

3.3. Interface strength

The strength of the interfaces was derived from the cleavage calculations. These were performed for the cleavage plane perpendicular to the considered interface (see Fig. 6d), as well as along the interface planes considering different interface orientations, and cleavage planes (parallel to the interface) in the superlattice (i.e., not only along the interface). Examples of the excess energy $\Delta E(x)$ (fitted with Eq. 1) and applied stress $\sigma(x) = d\Delta E(x)/dx$ as a function of the separation x are shown in Fig. 6a–c for the case of cleaving perpendicular to the interface for different magnetic states of CrN in (100)-orientated CrN/TiN.

Several observations can be made. Firstly, the cleavage energies are reasonably converged for the maximum separation of 10 Å. Secondly, the fit with Eq. 1 approximates the data well. Finally, there is no significant difference between afm-CrN/TiN (Fig. 6a), fm-CrN/TiN (Fig. 6b) and the pm-CrN/TiN (Fig. 6c) configurations.

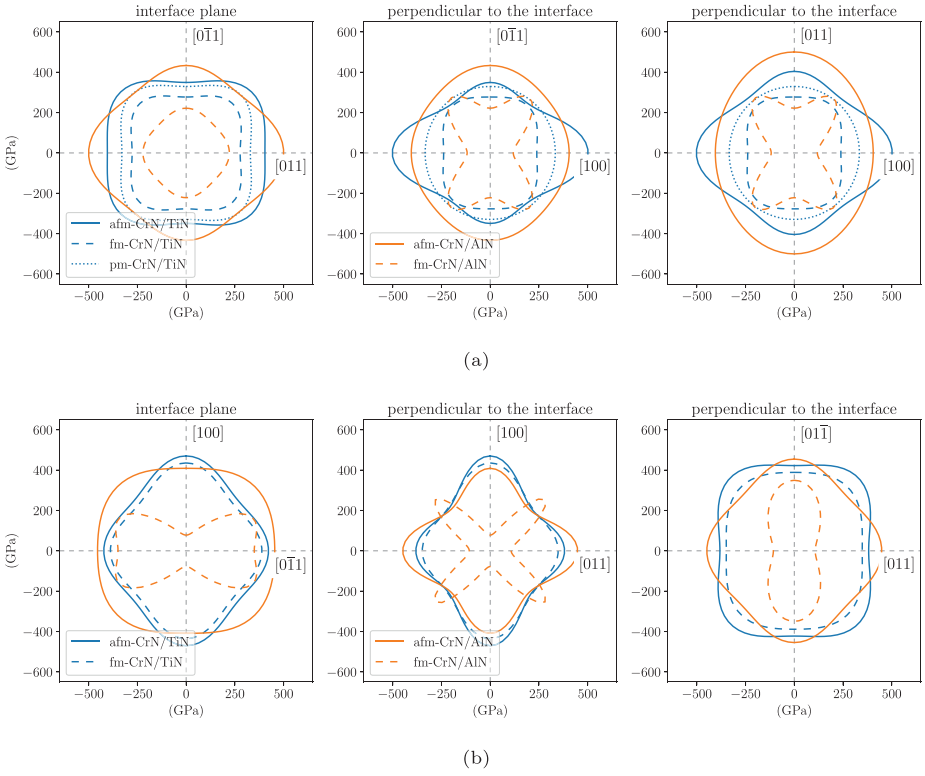

Fig. 5. Directional Young's modulus for the three main projection planes of CrN/TiN and CrN/AlN with a) (100) and b) (011) interfaces. Various magnetic states were considered: solid, dashed and dotted lines represent afm-, fm-, and pm-CrN configuration, respectively.

All three cases yield comparable parameters, E_c (cleavage energy for large gap distance), critical length l_c and critical stress σ_{crit}.

The results for various cleavage planes and material systems cleaved parallel to the interface are summarized in Fig. 7. The figures show both the cleavage energy, E_c, and the critical stress, σ_{crit}, for the interface and all parallel planes in the supercell, for fm and afm state of CrN, for the two interface orientations (100) and (110), and both CrN/TiN and CrN/AlN systems. At a first glance one can immediately make three observations: the values fluctuate depending on the actual cleavage plane, the actual magnetic state does not influence the values significantly (fm and afm cleavage properties are qualitatively, and often also quantitatively almost overlapping), and the critical stress and the cleavage energy mostly follow each other. The latter can be expected since both high critical stress and high cleavage energy are related to the greater bond strengths. The (100) pm-CrN/TiN, which was cleaved just at the interface, fits into this trend as well with $E_c = 2.9\,\text{J/m}^2$ and $\sigma_c = 29.5\,\text{GPa}$.

Regarding the oscillatory behaviour, this was already shown in similar studies on different material systems [25,26] and can be linked to Friedel oscillations in the electron charge density due to the interfaces [53]. Since the interface breaks translation symmetry, mobile charge tends to screen this perturbation. This process is in general much more efficient in metallic systems (TiN, CrN) having free electrons, than in semiconductors (AlN), the latter thus showing only very weak charge oscillations. Eventually, the charge oscillations lead to local strengthening/weakening of interplanar bonds, and hence directly affect the cleavage properties. Importantly, the interface is not necessarily the weakest link in terms of tensile strength (see, e.g., CrN/TiN (100) superlattice in Fig. 7b). Nevertheless, comparing the superlattice cleavage properties with values for bulk materials (solid horizontal lines), none of the systems is predicted to be superior to both of the individual homogeneous materials: the lowest critical stress of the superlattices (the weakest link) is always smaller than the critical stress of at least one of the bulks. Such behaviour is in line with other nitride superlattices [25,26]. This holds true also for the direction perpendicular to the interfaces (cf. values in Figs. 6 and 7), at least for the investigated bi-layer period.

3.4. Fracture toughness

The stress intensity factor, K_{IC}, was calculated for different superlattice configurations according to Eq. (3) using the stiffness constants (Tab. 2) and the minimal cleavage energies from previous section. The values are shown in Fig. 8. The blue and orange bars represent the (100) and (110) interfaces, respectively. Reference values for the binary nitrides are shown with the pale colours. Additional values corresponding to crack propagation planes perpendicular to the interfaces are marked with the hatched pattern. For clarity, each configuration is further labelled with the Miller indices of the crack surfaces.

The superlattice K_{IC} values never exceed the values of the corresponding binary systems (note that a fair comparison includes the same crack surfaces!). In the case of the (100) interfaces, the SL values lie always between the limits set by the binary nitrides. Contrarily, the K_{IC} SL values are lower than the corresponding binaries for the (011) orientated interfaces. This could indicate that the superlattice effect—K_{IC} values superior to the binary compounds [17,18]—reaches the maximum enhancement for different bi-layer period Λ depending on the orientation of the SL interface. Such speculation would require further analysis and likely also employment of methods beyond DFT. For the (110) directions the binaries show higher fracture toughness compared to superlattices this is because the cleavage energies are lower for the supercells than the ones of the binaries. Our results further suggest that cleaving the (100) planes is easier than the (011) planes. This is somewhat surprising result taking into account that the (100) direction is the

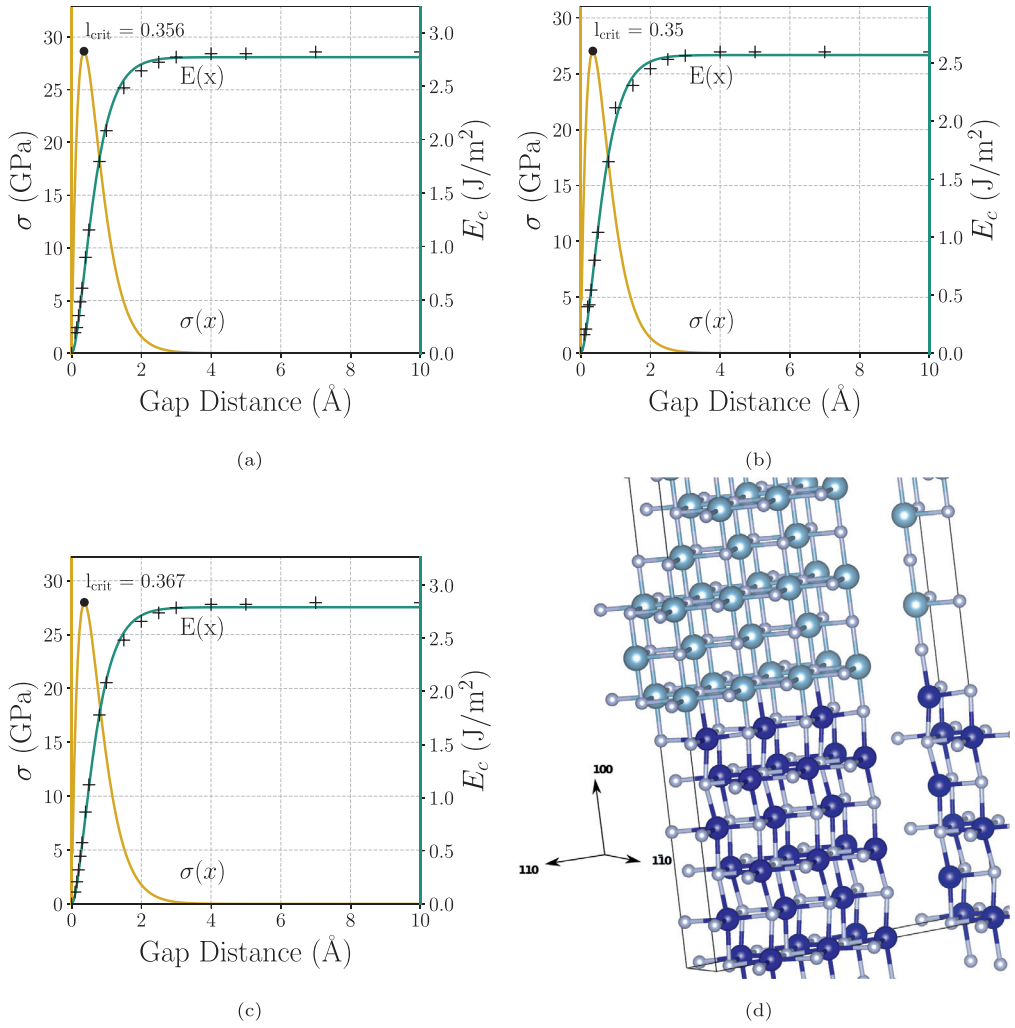

Fig. 6. Critical stresses and cleavage energies for cleavages, perpendicular to the interface (100) along the [010] direction of a) afm- b) fm- (100) and c) pm-CrN/TiN. In contrast to the cleavage in interface direction where differences between the different magnetic states occur perpendicular to the interface the magnetic configuration does not play a great role. d) The CrN/TiN supercell cleaved perpendicular to the (100) interface. The structures were visualized using the VESTA3 software [38].

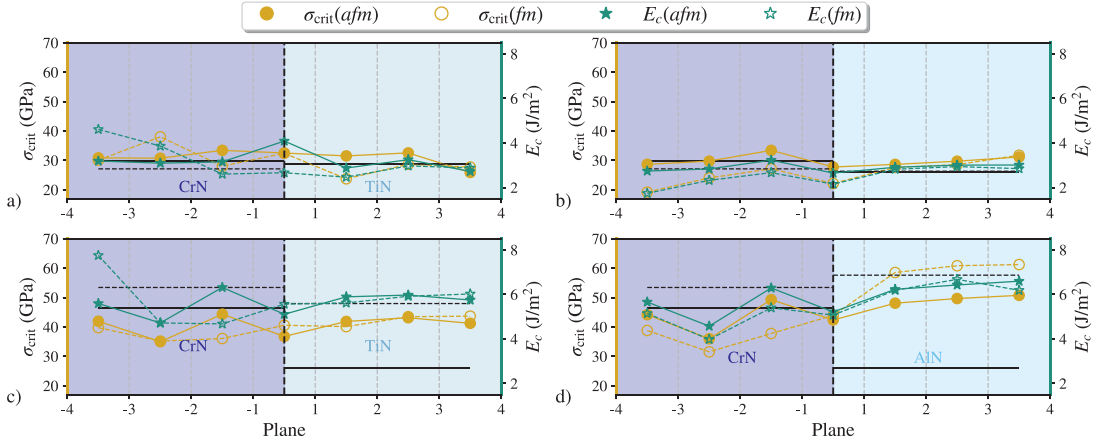

Fig. 7. The critical stress (yellow) and the cleavage energy (green) for different material systems and interface orientations. The full and dashed lines correspond to the afm and fm magnetic state of CrN. a) shows the values for CrN/TiN with the (100) interface, b) CrN/AlN with the (100) interface, c) CrN/TiN with the (011) interface and d) CrN/AlN with the (011) interface. The horizontal lines denote the critical (solid lines) stress and the cleavage energy (dashed lines) for bulk afm-CrN and TiN/AlN as reference values for the SLs. (For interpretation of the references to colour in this figure legend, the reader is referred to the web version of this article.)

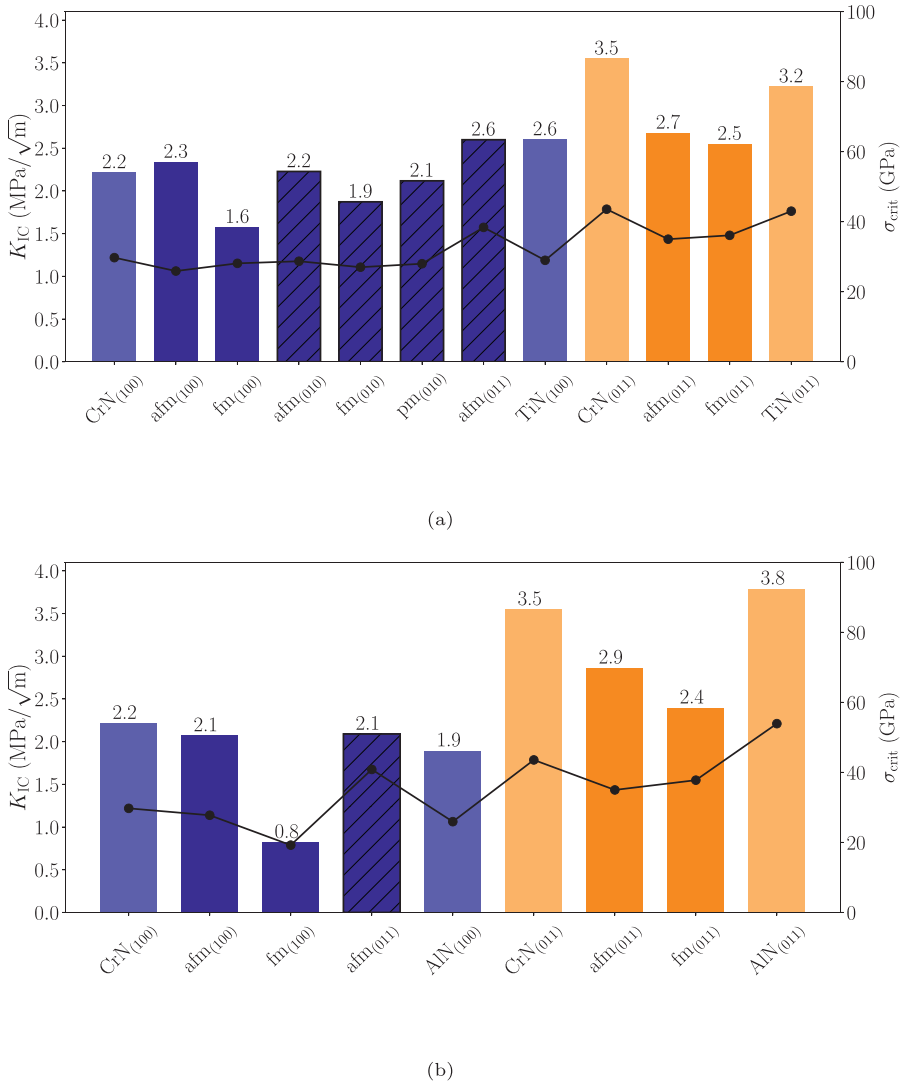

Fig. 8. Fracture toughness (K_{IC} for the a) CrN/TiN and b) CrN/AlN. The blue bars represent the (100), the orange ones the (011) interface. The black boarder denotes the fracture toughness perpendicular to the interface, the so created surface is denoted in the labels. In both material combinations the (100) direction shows similar fracture toughness of the binaries and the superlattices even for the different fracture orientations and magnetic configurations. The (110) interface on the other hand sees a decrease in the K_{IC} compared ot the binaries. (For interpretation of the references to colour in this figure legend, the reader is referred to the web version of this article.)

stiffest for both CrN and TiN (see Fig. 4). According to Eq. (3), K_{IC} depends apart from the directional Young's modulus also on the corresponding surface energy (in our case approximated by the cleavage energy). Therefore, the plane with the lowest cleavage energy, becomes the decisive one (i.e. the weakest link) for the fracture toughness. The results in Fig. 7 clearly show, that the interface itself is not necessarily the weakest link: while E_c reaches a minimum at the interface in the afm-(100)CrN/AlN case, the minimum is predicted to be in the CrN layer in the afm-(011)CrN/AlN case (as well as in both fm-CrN/AlN cases). The factor limiting fracture toughness of CrN/TiN is TiN in the case of (100) interfaces but it is the CrN in the case of (011) interfaces.

The black data points and lines in Fig. 8 represent corresponding σ_{crit} values. We see a qualitative agreement with the K_{IC} profile. This is not surprising since E_c and σ_{crit} are related (Eq. 2), and as discussed above, E_c is the decisive quantity for the K_{IC} in the case when E_{hkl} is not vastly differing over the SL constituents. Consequently, high (minimum) critical stress can be used as an indicator for high fracture toughness.

A final comment concerns various magnetic configurations. The room temperature state of CrN is paramagnetic. Zhou et al. [30] suggested that (computationally cheaper) fm-CrN yields reasonable approximation for elasticity of pm-CrN. Inspecting the significantly lower K_{IC} values of the fm-CrN/TiN and fm-CrN/AlN SLs as compared with afm (and pm-CrN/TiN(010)), we conclude that the ferromagnetic state is not a reasonable approximation for fracture toughness. The underestimation of K_{IC} values can be traced to reduced cleavage properties in the fm state (Fig. 7). Although not so pronounced, such trend is obtained also for the cleavage planes perpendicular to the interface (Fig. 6) where the fm configuration yields both E_c and σ_{crit} lower than both afm and pm states.

4. Discussion

4.1. Stability of the afm-(100) state

The results in Section 3.1 revealed an unexpected behaviour of fm-(100)CrN/AlN SL: stabilization of a "false" afm state (see Fig. 2c). In Fig. 9 we show the development of individual magnetic moments of all Cr atoms during the cleavage process along various planes. The panels b and c corresponding to cleaving between CrN planes −1 and −2, and −2 and −3, respectively, demonstrate that

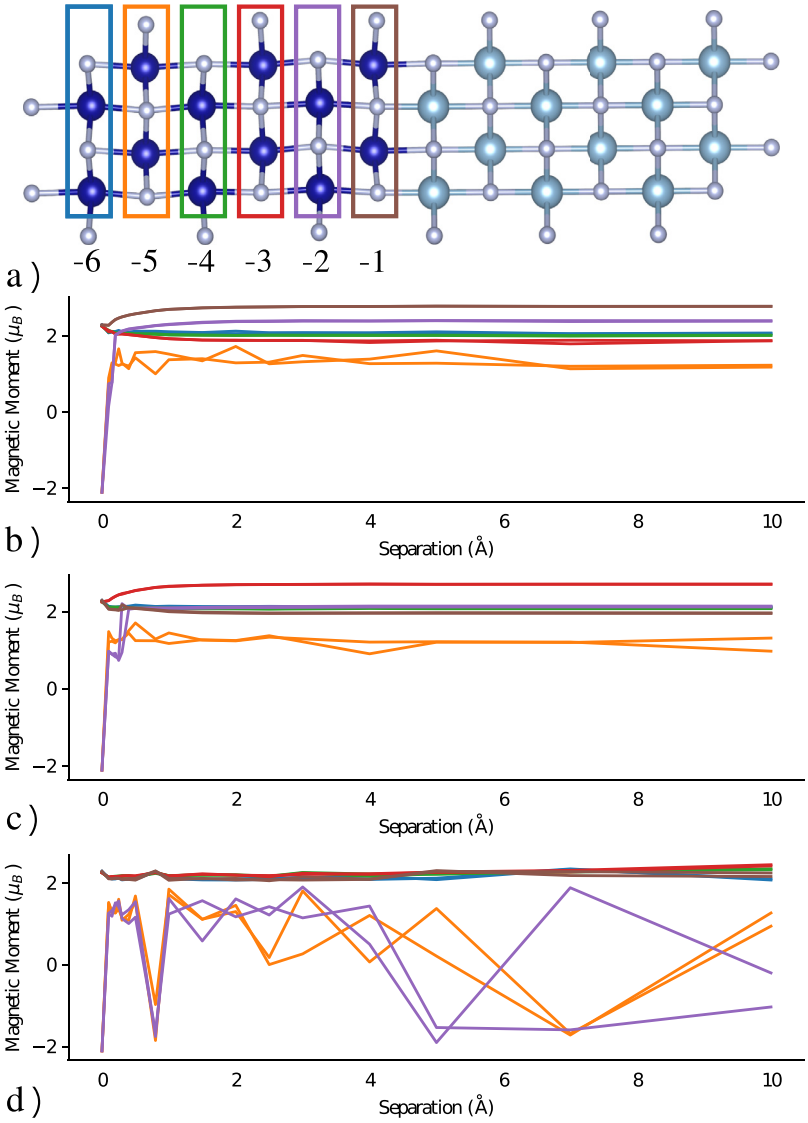

Fig. 9. Development of the magnetic moments of the Cr atoms in fm CrN/AlN with (100) interface for the different cleaving steps. a) the colored lines correspond to the colors used in the other plot to highlight the positions of the different Cr atoms, the dashed lines indicate the cleavage planes. b) cleaved between the planes -1 and -2, c) cleaved between the planes -2 and -3 and d) cleaved between the planes -3 and -4. Cr in the same planes have the same colors.

as soon as the symmetry of the modelling box is broken by introducing extra spacing between the planes, the anti-parallel orientated spins turn back into the fm-configuration (or, similarly, that the flipping to the false afm-(100) state does not occur). On the contrary, when cleaving the SLs right in the middlle of the CrN block, hence preserving the mirror symmetry of the model, the resulting system seems to alternate between two, presumably energetically almost identical, states, namely fm or afm-(100). Even more interestingly, as soon as the separation exceeds ≈ 1.5 Å, the behaviour of -2 (violet) and -5 (orange) planes becomes uncorrelated (independent), meaning that the magnetic interaction causing the magnetic order is becomes negligible. Those results suggest that the afm-(100) magnetic state is both a surface/interface-induced and symmetry-stabilized phenomenon.

4.2. Interplay between strength and magnetism

Starting from the cubic rock-salt lattice, CrN lowers its symmetry firstly by the antiferromagnetic order, which in turn leads to the orthorhombic structure [30]. Inspecting the directional Young's modulus (e.g., the green dashed lines in Fig. 4) yields $E_{[011]}(\mathrm{CrN}) > E_{[0\bar{1}1]}(\mathrm{CrN})$. Recalling that the afm order consists of alternating (011) double-planes with the same spin orientation (Fig. 1), one is tempted to ascribe the increased Young's modulus in the [011] direction to an attractive spin interaction between oppositely-orientated spins: while the Cr-Cr chains (first nearest Cr-Cr pairs) along the $[0\bar{1}1]$ consist of atoms with the same spin orientation, the Cr-Cr chains along the [011] direction contain anti-parallel spins on the Cr nearest neighbours. This speculation about magnetic-spin attraction can be further supported by inspecting the cleavage properties in Fig. 6d. The lowest critical stress and cleavage energy are obtained for cleaving between planes -2 and -3, which have same-orientated spin (Fig. 3d). On the other hand, cohesion between planes -3 and -4, and -2 and -1, in each case with oppositely orientated spins, is clearly higher.

4.3. Experimental evidence

To support our theoretical analysis, a series of CrN/TiN superlattices were produced with a DC reactive magnetron sputtering process in a AJA Orion 5 deposition plant equipped with 3″ Ti and a 2″ Cr target (both from Plansee Composite Materials GmbH).

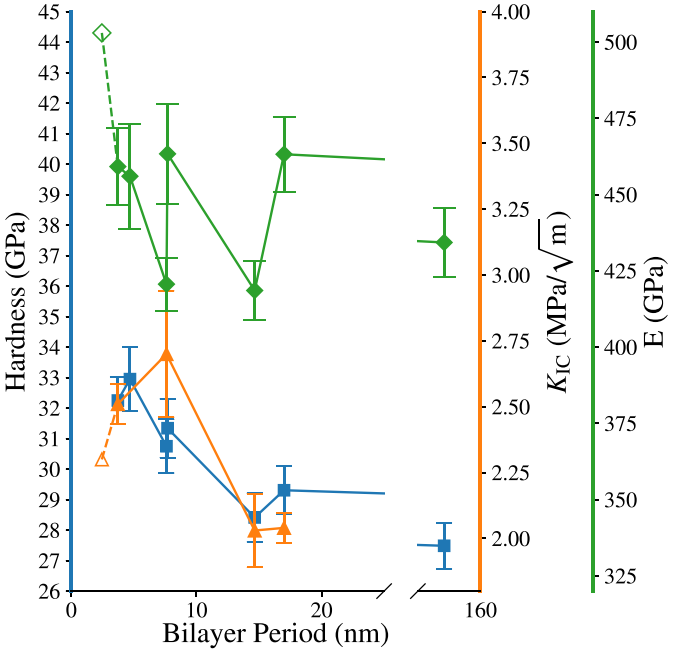

Fig. 10. Results of the micro mechanical experiments on CrN/TiN thin films. The hardness (blue squares) of the coatings increases to its maximum at a bi-layer period of 4.7 nm and falls off afterwards. The fracture toughness (orange triangles) has a similar shape to the hardness with an increase until 7.6 nm and a drop afterwards. The Young's modulus (green diamonds) exhibits fluctuating values for the different bi-layer periods. For the fracture toughness and the Young's modulus the calculated values are presented by the star symbols. (For interpretation of the references to colour in this figure legend, the reader is referred to the web version of this article.)

Prior to deposition, the substrates (MgO (100) to ensure epitaxial growth) were cleaned in acetone and ethanol for 5 minutes each, transferred to the vacuum chamber (base pressure below 2×10^{-4} Pa), heated to the deposition temperature of 700° C, and finally Argon ion etched for 10 minutes at a working gas pressure of 6 Pa. The deposition of the substrates (rotating at 1 min^{-1}) was performed at a working gas (7:3 sccm Nitrogen and Argon mixture) pressure of 0.4 Pa. After this process the substrates were passively cooled down to a temperature below 50° C. Films with nominal bi-layer periods between 2 and 200 nm were synthesized. The hardness and the Young's modulus of the coatings were determined by nanoindentation using a Fisher-Cripps UMIS indentation system, equipped with a diamond Berkovich tip, after the method described by Oliver and Pharr [54]. To measure the fracture toughness, pre-notched cantilevers were machined with a focused ion beam (FEI Quanta 200 3D dual beam focused ion beam) from the coatings, following a procedure described in [55]. The cut beams were then displaced *in situ* with a nanoindenter (Hysitron PI-85) with a spherical tip at 5 nm/s inside a SEM (FEI Quanta 250 FEGSEM). From the forces and the geometry, the fracture toughness (stress intensity factor, K_{IC}) was calculated using the equation as

$$K_{IC} = \frac{F_{max} l}{b w^{\frac{3}{2}}} f\left(\frac{a}{w}\right) \tag{6}$$

where the geometry factor f is taken from [56] as

$$f\left(\frac{a}{w}\right) = 1.46 + 24.36\frac{a}{w} - 47.21\left(\frac{a}{w}\right)^2 + 75.18\left(\frac{a}{w}\right)^3. \tag{7}$$

Fig. 10 shows the experimental results for the hardness, fracture toughness and Young's modulus plot against the bi-layer period. Both, hardness, H, and fracture toughness, K_{IC}, exhibit the superlattice effect by peaking at small bi-layer period, similarly to previously reported behaviour for other superlattices, CrN/TiN [17], TiN/WN [18] or MoN/TaN [19]. The hardness reaches maximum of 32.2 GPa for a bi-layer period of 4.7 nm, after which it decreases quickly to 28.4 GPa at 14.7 nm and then further decreases to 27.5 GPa at 157 nm. The fracture toughness shows a similar trend. It peaks with 2.7 MPa/$\sqrt{m}$ at a bi-layer period of 7.6 nm and decreases afterwards towards 2 MPa/$\sqrt{m}$. It is important to note that the K_{IC} measurements at the peak have a high standard deviation.

The absolute values for K_{IC} are in good agreement with the DFT data presented in this study. Considering that the crack in the experiment propagated perpendicular to the interfaces, the relevant values for the afm-(100)CrN/TiN system are 2.2 and 2.6 MPa/$\sqrt{m}$ for (010) and (011) fracture planes. The extrapolated experimental data trend to this small bi-layer period range fall in-between those two theoretical values. The indentation modulus values in Fig. 10 fluctuate between ≈ 420 and ≈ 463 GPa. The calculated values are in decent agreement with E_{100} for afm-(100)CrN/TiN (503 GPa). Although not an exhaustive proof, these good correlations between theoretical predictions and experimentally measured values of mechanical properties demonstrate on the one hand that the rather small atomistic models are relevant for modelling nitride superlattices (including magnetism) and, on the other hand, they are capable of predicting not only trends, but often also quantitative values.

5. Conclusions

In the present work we have presented a comprehensive study on the impact of interface orientation and magnetic state of CrN/TiN and CrN/AlN cubic superlattices with a bi-layer period of ≈ 2.5 nm on their structural and mechanical properties. Similarly to previous studies, also here interlayer distance oscillations appeared, mostly in the metallic (TiN, CrN) layers. Those were related to interface-induced Friedel charge oscillations. Analysis of local magnetic moments suggested that there is no correlation between those interplanar distances and magnetic moments on Cr atoms.

Next we discussed elastic properties of the superlattices. We could show that explicitly including interfaces is important, although in many cases the computationally much more efficient continuum-mechanics based approach of Grimsditsh and Nizzoli brings sufficiently accurate results. Importantly, a hypothetical ferromagnetic state yields not only the softest elastic response, but also a different symmetry of it with a very strong anisotropic character. This effectively rules out the fm state as an approximation for (computationally much more demanding) paramagnetic state of CrN.

Lastly we calculated fracture toughness, K_{IC}. Although none of our geometries showed a superlattice effect, i.e. values exceeding those of binary constituent materials, a comparison with experimental data suggested not only qualitative but also quantitative agreement. The studied superlattice bi-layer period of ≈ 2.5 nm, mostly limited by the computationally expensive quantum mechanical treatment, is smaller than that for which K_{IC} (and also hardness) experimentally show the peak.

Declaration of Competing Interest

We wish to confirm that there are no known conflicts of interest associated with this publication and there has been no significant financial support for this work that could have influenced its outcome.

Acknowledgements

The authors greatly acknowledge financial support from Austrian Science Fund (P 30341-N36). LL and DH are also grateful for the financial support through Scientific & Technological Cooperation of the Austrian Agency for International Cooperation in Education and Research (WTZ-CZ-05/2018). The results presented were achieved using the Vienna Scientific Cluster (VSC).

References

[1] P.H. Mayrhofer, A. Hörling, L. Karlsson, J. Sjölén, T. Larsson, C. Mitterer, L. Hultman, Self-organized nanostructures in the Ti–Al–N system, Appl. Phys. Lett. 83 (10) (2003) 2049–2051, doi:10.1063/1.1608464.
[2] Ritchie R. O., The conflicts between strength and toughness, Nature Materials 10 (11) 817-822, doi:10.1038/nmat3115.
[3] C. Mitterer, 2.16 – PVD and CVD hard coatings, in: V.K. Sarin (Ed.), Comprehensive Hard Materials, Elsevier, Oxford, 2014, pp. 449–467, doi:10.1016/B978-0-08-096527-7.00035-0.
[4] C.M. Koller, R. Hollerweger, C. Sabitzer, R. Rachbauer, S. Kolozsvári, J. Paulitsch, P.H. Mayrhofer, Thermal stability and oxidation resistance of arc evaporated TiAlN, TaAlN, TiAlTaN, and TiAlN/TaalN coatings, Surf. Coat. Technol. 259, Part C (2014) 599–607, doi:10.1016/j.surfcoat.2014.10.024.
[5] Y.X. Xu, L. Chen, F. Pei, Y. Du, Y. Liu, J.L. Yue, Influence of hf on the structure, thermal stability and oxidation resistance of Ti-Al-N coatings, Thin Solid Films 565 (2014) 25–31, doi:10.1016/j.tsf.2014.06.043.
[6] R. Hollerweger, H. Riedl, M. Arndt, S. Kolozsvári, S. Primig, P.H. Mayrhofer, Guidelines for increasing the oxidation resistance of Ti-Al-N based coatings, Thin Solid Films 688 (2019) 137290, doi:10.1016/j.tsf.2019.05.009.
[7] F. Guo, J. Wang, Y. Du, D. Holec, P. Ou, H. Zhou, L. Chen, Y. Kong, Structural evolution of oxygen on the surface of TiAlN: Ab initio molecular dynamics simulations, Appl. Surf. Sci. 470 (2019) 520–525, doi:10.1016/j.apsusc.2018.11.158.
[8] H. Lind, F. Tasnádi, I.A. Abrikosov, Systematic theoretical search for alloys with increased thermal stability for advanced hard coatings applications, New J. Phys. 15 (9) (2013) 095010, doi:10.1088/1367-2630/15/9/095010.
[9] P.H. Mayrhofer, R. Rachbauer, D. Holec, F. Rovere, J.M. Schneider, 4.14 – Protective Transition Metal Nitride Coatings, in: S. Hashmi, G.F. Batalha, C.J.V. Tyne, B. Yilbas (Eds.), Comprehensive Materials Processing, Elsevier, Oxford, 2014, pp. 355–388, doi:10.1016/B978-0-08-096532-1.00423-4.
[10] H. Bolvari, M. to Baben, F. Nahif, D. Music, V. Schnabel, K.P. Shaha, S. Mraz, J. Bednarcik, J. Michalikova, J.M. Schneider, Effect of si additions on thermal stability and the phase transition sequence of sputtered amorphous alumina thin films, J. Appl. Phys. 117 (2015) 025302, doi:10.1063/1.4905296.
[11] M. to Baben, M. Hans, D. Primetzhofer, S. Evertz, H. Ruess, J.M. Schneider, Unprecedented thermal stability of inherently metastable titanium aluminum nitride by point defect engineering, Mat. Res. Lett. 5 (3) (2017) 158–169, doi:10.1080/21663831.2016.1233914.
[12] P.H. Mayrhofer, C. Mitterer, L. Hultman, H. Clemens, Microstructural design of hard coatings, Prog. Mater. Sci. 51 (8) (2006) 1032–1114, doi:10.1016/j.pmatsci.2006.02.002.
[13] S. Veprek, A.S. Argon, R.F. Zhang, Origin of the hardness enhancement in superhard nc-TiN/a-Si3N4 and ultrahard nc-TiN/a-Si_3N_4/$TiSi_2$ nanocomposites, Philos. Mag. Lett. 87 (12) (2007) 955–966, doi:10.1080/09500830701666139.
[14] J. Zalesak, M. Bartosik, R. Daniel, C. Mitterer, C. Krywka, D. Kiener, P.H. Mayrhofer, J. Keckes, Cross-sectional structure-property relationship in a graded nanocrystalline $Ti_{1-x}Al_xN$ thin film, Acta Mater. 102 (2016) 212–219, doi:10.1016/j.actamat.2015.09.007.
[15] N. Ghafoor, I. Petrov, D. Holec, G. Greczynski, J. Palisaitis, P.O.A. Persson, L. Hultman, J. Birch, Self-structuring in $Zr_{1-x}Al_xN$ films as a function of composition and growth temperature, Sci. Rep. 8 (1) (2018) 16327, doi:10.1038/s41598-018-34279-w.
[16] U. Helmersson, S. Todorova, S. Barnett, J.-E. Sundgren, L. Markert, J. Greene, Growth of single-crystal TiN/VN strained-layer superlattices with extremely high mechanical hardness, J. Appl. Phys. 62 (2) (1987) 481–484, doi:10.1063/1.339770.
[17] R. Hahn, M. Bartosik, R. Soler, C. Kirchlechner, G. Dehm, P. Mayrhofer, Superlattice effect for enhanced fracture toughness of hard coatings, Scr. Mater. 124 (2016) 67–70, doi:10.1016/j.scriptamat.2016.06.030.
[18] J. Buchinger, N. Koutná, Z. Chen, Z. Zhang, P.H. Mayrhofer, D. Holec, M. Bartosik, Toughness enhancement in TiN/WN superlattice thin films, Acta Mater. 172 (2019) 18–29, doi:10.1016/j.actamat.2019.04.028.
[19] R. Hahn, N. Koutná, T. Wójcik, A. Davydok, S. Kolozsvári, C. Krywka, D. Holec, M. Bartosik, P.H. Mayrhofer, Mechanistic study of superlattice-enabled high toughness and hardness in MoN/TaN coatings, Commun. Mater. 1 (1) (2020) 62, doi:10.1038/s43246-020-00064-4.
[20] S. Nikolov, M. Petrov, L. Lymperakis, M. Friák, C. Sachs, H.-O. Fabritius, D. Raabe, J. Neugebauer, Revealing the design principles of high-performance biological composites using ab initio and multiscale simulations: the example of lobster cuticle, Adv. Mater. 22 (4) (2010) 519–526, doi:10.1002/adma.200902019.
[21] M. Meindlhumer, J. Zalesak, R. Pitonak, J. Todt, B. Sartory, M. Burghammer, A. Stark, N. Schell, R. Daniel, J.F. Keckes, M. Lessiak, A. Köpf, R. Weißenbacher, J. Keckes, Biomimetic hard and tough nanoceramic Ti-Al-N film with self-assembled six-level hierarchy, Nanoscale 11 (16) (2019) 7986–7995, doi:10.1039/c8nr10339a.
[22] R. Daniel, M. Meindlhumer, W. Baumegger, J. Todt, J. Zalesak, T. Ziegelwanger, C. Mitterer, J. Keckes, Anisotropy of fracture toughness in nanostructured ceramics controlled by grain boundary design, Mater. Des. 161 (2019) 80–85, doi:10.1016/j.matdes.2018.11.028.
[23] M. Schlögl, B. Mayer, J. Paulitsch, P.H. Mayrhofer, Influence of CrN and AlN layer thicknesses on structure and mechanical properties of CrN/AlN superlattices, Thin Solid Films 545 (2013) 375–379, doi:10.1016/j.tsf.2013.07.026.
[24] P. Lazar, J. Redinger, R. Podloucky, Density functional theory applied to VN/TiN multilayers, Phys. Rev. B Condens. Matter 76 (2007) 174112, doi:10.1103/PhysRevB.76.174112.
[25] P. Řehák, M. Černý, D. Holec, Interface-induced electronic structure toughening of nitride superlattices, Surf. Coat. Technol. 325 (2017) 410–416, doi:10.1016/j.surfcoat.2017.06.065.
[26] N. Koutná, P. Řehák, Z. Chen, M. Bartosik, M. Fallmann, M. Černý, Z. Zhang, M. Friák, M. Šob, P.H. Mayrhofer, D. Holec, Correlating structural and mechanical properties of AlN/TiN superlattice films, Scr. Mater. 165 (2019) 159–163, doi:10.1016/j.scriptamat.2019.02.021.
[27] N. Koutná, R. Hahn, J. Zálešák, M. Friák, M. Bartosik, J. Keckes, M. Šob, P.H. Mayrhofer, D. Holec, Point-defect engineering of MoN/TaN superlattice films: a first-principles and experimental study, Mater. Des. 186 (2020) 108211, doi:10.1016/j.matdes.2019.108211.
[28] F. Wang, D. Holec, M. Odén, F. Mücklich, I.A. Abrikosov, F. Tasnádi, Systematic ab initio investigation of the elastic modulus in quaternary transition metal nitride alloys and their coherent multilayers, Acta Mater. 127 (2017) 124–132, doi:10.1016/j.actamat.2017.01.017.
[29] L.M. Corliss, N. Elliott, J.M. Hastings, Antiferromagnetic structure of CrN, Phys. Rev. 117 (4) (1960) 929–935, doi:10.1103/PhysRev.117.929.
[30] L. Zhou, F. Körmann, D. Holec, M. Bartosik, B. Grabowski, J. Neugebauer, P.H. Mayrhofer, Structural stability and thermodynamics of CrN magnetic phases from ab initio calculations and experiment, Phys. Rev. B. 90 (18) (2014) 184102, doi:10.1103/PhysRevB.90.184102.
[31] Z. Zhang, X. Gu, D. Holec, M. Bartosik, P.H. Mayrhofer, H.P. Duan, Superlattice-induced oscillations of interplanar distances and strain effects in the CrN/AlN system, Phys. Rev. B Condens. Matter 95 (15) (2017) 155305, doi:10.1103/PhysRevB.95.155305.
[32] M. Friák, D. Tytko, D. Holec, P.-P. Choi, P. Eisenlohr, D. Raabe, J. Neugebauer, Synergy of atom-probe structural data and quantum-mechanical calculations in a theory-guided design of extreme-stiffness superlattices containing metastable phases, New J. Phys. 17 (9) (2015) 093004, doi:10.1088/1367-2630/17/9/093004.
[33] A. Madan, I.W. Kim, S.C. Cheng, P. Yashar, V.P. Dravid, S.A. Barnett, Stabilization of cubic AlN in epitaxial AlN/TiN superlattices, Phys. Rev. Lett. 78 (9) (1997) 1743–1746, doi:10.1103/PhysRevLett.78.1743.
[34] V. Chawla, D. Holec, P. Mayrhofer, Stabilization criteria for cubic AlN in TiN/AlN and CrN/AlN bi-layer systems, J. Phys. D Appl. Phys. 46 (2013) 045305, doi:10.1088/0022-3727/46/4/045305.
[35] K. Yaddanapudi, First-principles study of structural phase transformation and dynamical stability of cubic AlN semiconductors, AIP Adv. 8 (2018) 125006, doi:10.1063/1.5054697.
[36] F. Rivadulla, M. Bãobre-López, C.X. Quintela, A. Pïeiro, V. Pardo, D. Baldomir, M.A. López-Quintela, J. Rivas, C.A. Ramos, H. Salva, J.S. Zhou, J.B. Goodenough, Reduction of the bulk modulus at high pressure in CrN, Nat. Mater. 8 (12) (2009) 947–951, doi:10.1038/nmat2549.
[37] J.E. Sundgren, B.O. Johansson, S.E. Karlsson, H.T. Hentzell, Mechanisms of reactive sputtering of titanium nitride and titanium carbide II: morphology and structure, Thin Solid Films 105 (4) (1983) 367–384, doi:10.1016/0040-6090(83)90319-X.
[38] K. Momma, F. Izumi, VESTA3 For three-dimensional visualization of crystal, volumetric and morphology data, J. Appl. Crystallogr. 44 (6) (2011) 1272–1276, doi:10.1107/S0021889811038970.
[39] G. Kresse, D. Joubert, From ultrasoft pseudopotentials to the projector augmented-wave method, Phys. Rev. B. 59 (3) (1999) 1758–1775, doi:10.1103/PhysRevB.59.1758.
[40] G. Kresse, J. Furthmüller, Efficient iterative schemes for *ab initio*total-energy calculations using a plane-wave basis set, Phys. Rev. B. 54 (16) (1996) 11169–11186, doi:10.1103/PhysRevB.54.11169.
[41] A. van de Walle, P. Tiwary, M. de Jong, D.L. Olmsted, M. Asta, A. Dick, D. Shin, Y. Wang, L.Q. Chen, Z.K. Liu, Efficient stochastic generation of special quasirandom structures, Calphad 42 (2013) 13–18, doi:10.1016/j.calphad.2013.06.006.
[42] R. Yu, J. Zhu, H. Ye, Calculations of single-crystal elastic constants made simple, Comput. Phys. Commun. 181 (3) (2010) 671–675, doi:10.1016/j.cpc.2009.11.017.
[43] M. Moakher, A.N. Norris, The closest elastic tensor of arbitrary symmetry to an elasticity tensor of lower symmetry, J. Elast. 85 (3) (2006) 215–263, doi:10.1007/s10659-006-9082-0.
[44] M. Friák, W.A. Counts, D. Ma, B. Sander, D. Holec, D. Raabe, J. Neugebauer, Theory-guided materials design of multi-phase Ti-Nb alloys with bone-matching elastic properties, Materials (Basel) 5 (10) (2012) 1853–1872, doi:10.3390/ma5101853.
[45] T. Hickel, U. Aydin, M. Friák, D. Ma, D. Raabe, J. Neugebauer, Self-consistent scale-bridging approach to compute the elasticity of multi-phase polycrystalline materials, MRS Online Proceedings Library Archive 1524 (2013), doi:10.1557/opl.2013.41.

[46] M. Grimsditch, F. Nizzoli, Effective elastic constants of superlattices of any symmetry, Phys. Rev. B Condens. Matter 33 (8) (1986) 5891–5892, doi:10.1103/PhysRevB.33.5891.
[47] J.H. Rose, J.R. Smith, J. Ferrante, Universal features of bonding in metals, Phys. Rev. B Condens. Matter 28 (4) (1983) 1835–1845, doi:10.1103/PhysRevB.28.1835.
[48] Ohring M. Materials Science of Thin Films, Academic Press (2002), doi:10.1016/B978-0-12-524975-1.X5000-9.
[49] J.F. Nye, Physical properties of crystals, Clarendon Press, Oxford, 1957.
[50] M. Zhang, J. He, Ab-initio calculation of elastic constants of TiN, Surf. Coat. Technol. 142–144 (2001) 125–131, doi:10.1016/S0257-8972(01)01221-X.
[51] U.P. Verma, P.S. Bisht, Ab-initio study of AlN in zinc-blende and rock-salt phases, Solid State Sci. 12 (5) (2010) 665–669, doi:10.1016/j.solidstatesciences.2008.12.002.
[52] P.H. Mayrhofer, D. Music, T. Reeswinkel, H.G. Fuß, J.M. Schneider, Structure, elastic properties and phase stability of $Cr_{1-x}Al_xN$, Acta Mater. 56 (11) (2008) 2469–2475, doi:10.1016/j.actamat.2008.01.054.
[53] R.F. Zhang, A.S. Argon, S. Veprek, Friedel oscillations are limiting the strength of superhard nanocomposites and heterostructures, Phys. Rev. Lett. 102 (1) (2009) 015503, doi:10.1103/PhysRevLett.102.015503.
[54] W. Oliver, G. Pharr, An improved technique for determining hardness and elastic modulus using load and displacement sensing indentation experiments, J. Mater. Res. 7 (6) (1992) 1564–1583, doi:10.1557/jmr.1992.1564.
[55] R. Hahn, M. Bartosik, M. Arndt, P. Polcik, P.H. Mayrhofer, Annealing effect on the fracture toughness of CrN/TiN superlattices, Int. J. Refract. Met. Hard Mater 71 (2018) 352–356, doi:10.1016/j.ijrmhm.2017.11.008.
[56] S. Brinckmann, K. Matoy, C. Kirchlechner, G. Dehm, On the influence of microcantilever pre-crack geometries on the apparent fracture toughness of brittle materials, Acta Mater. 136 (2017) 281–287, doi:10.1016/j.actamat.2017.07.014.